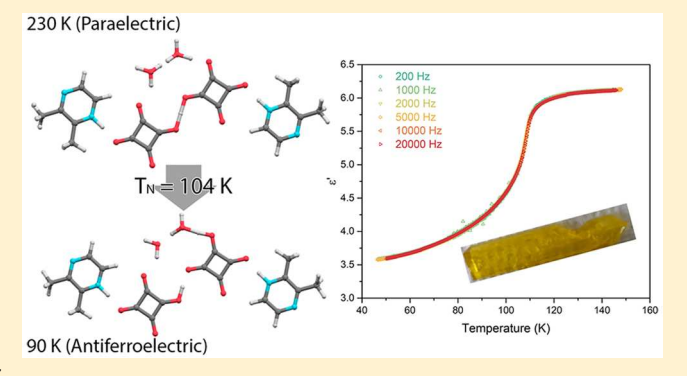


Antiferroelectric Phase Transition in a Proton-Transfer Salt of Squaric Acid and 2,3-Dimethylpyrazine

Jeff Lengyel, [†] Niaoping Wang, [‡] Eun Sang Choi, [§] Tiglet Besara, ^{§,○} Rico Schönemann, [§] Sanath Kumar Ramakrishna, ^{†,§} Jade Holleman, ^{§,||} Avery L. Blockmon, [⊥] Kendall D. Hughey, [⊥] Tianhan Liu, ^{||} Jacob Hudis, ^{||} Drake Beery, [†] Luis Balicas, ^{§,||} Stephen A. McGill, [§] Kenneth Hanson, [†] Janice L. Musfeldt, ^{⊥,#} Theo Siegrist, ^{§,∇} Naresh S. Dalal, ^{*,†,§} and Michael Shatruk, ^{*,†}

Supporting Information

ABSTRACT: A proton-transfer reaction between squaric acid (H₂sq) and 2,3-dimethylpyrazine (2,3-Me₂pyz) results in crystallization of a new organic antiferroelectric (AFE), (2,3- $Me_2pyzH^+)(Hsq^-)\cdot H_2O$ (1), which possesses a layered structure. The structure of each layer can be described as partitioned into strips lined with methyl groups of the Me₂pyzH⁺ cations and strips featuring extensive hydrogen bonding between the Hsq anions and water molecules. Variable-temperature dielectric measurements and crystal structures determined through a combination of single-crystal X-ray and neutron diffraction reveal an AFE ordering at 104 K. The phase transition is driven by ordering of protons within the hydrogen-bonded strips. Considering the extent of



proton transfer, the paraelectric (PE) state can be formulated as (2,3-Me₂pyzH⁺)₂(Hsq₂³⁻)(H₅O₂⁺), whereas the AFE phase can be described as (2,3-Me₂pyzH⁺)(Hsq⁻)(H₂O). The structural transition caused by the localization of protons results in the change in color from yellow in the PE state to colorless in the AFE state. The occurrence and mechanism of the AFE phase transition have been also confirmed by heat capacity measurements and variable-temperature infrared and Raman spectroscopy. This work demonstrates a potentially promising approach to the design of new electrically ordered materials by engineering molecule-based crystal structures in which hydrogen-bonding interactions are intentionally partitioned into quasi-onedimensional regions.

INTRODUCTION

Materials that exhibit electric ordering find important technological applications in ceramic capacitors, actuators, piezoelectric transducers, pyroelectric detectors, and sonars. They are also extensively investigated in the search for new types of functionality, for example, multiferroics.² While this area of research has been heavily dominated by inorganic materials, especially transition metal oxides,³ organic ferroelectrics have become much more notable since the early 2000s, especially due to discoveries of several remarkable organic ferroelectric materials⁵ whose performance figures of merit are comparable to those of the state-of-the-art inorganic ferroelectrics.6

Designing materials with electric ordering represents a nontrivial task. While phenomenologically analogous to ferroand antiferroelectrics, magnetic materials only require sufficiently strong magnetic exchange coupling between moments on interacting magnetic sites to undergo magnetic ordering below the critical temperature. On the other hand, ferroelectric (FE) materials require symmetry breaking in the

Received: April 25, 2019 Published: September 24, 2019

[†]Department of Chemistry and Biochemistry, Florida State University, 95 Chieftan Way, Tallahassee, Florida 32306, United States *Neutron Scattering Division, Neutron Sciences Directorate, Oak Ridge National Laboratory, Oak Ridge, Tennessee 37831, United

[§]National High Magnetic Field Laboratory, 1800 East Paul Dirac Drive, Tallahassee, Florida 32310, United States

Department of Physics, Florida State University, 77 Chieftan Way, Tallahassee, Florida 32306, United States

¹Department of Chemistry, University of Tennessee, 1420 Circle Drive, Knoxville, Tennessee 37996, United States

Department of Physics, University of Tennessee, 1408 Circle Drive, Knoxville, Tennessee 37996, United States

VDepartment of Chemical and Biomedical Engineering, FAMU-FSU College of Engineering, Tallahassee, Florida 32310, United States

crystal structure, with the formation of a polar space group, to transition from the disordered paraelectric (PE) phase to the ordered FE phase. In contrast to magnetic ordering, electric ordering generally requires concerted atomic displacements to achieve the breaking of space-group symmetry.8

The current interest in organic FEs is justified by both the low density of these materials and the high synthetic tunability of the molecular components that comprise them. The design of FE or antiferroelectric (AFE) organic solids generally relies on three different mechanisms: charge ordering, polar group ordering, or proton transfer. The latter is especially appealing, because the possibility of proton transfer is predictable and can occur with a high degree of cooperativity, which in turn can trigger abrupt FE or AFE ordering. A classic example of this behavior among inorganic materials is the ferroelectric transition in KH₂PO₄. Among organic ferroelectrics, noteworthy cases are FE ordering in croconic acid¹⁰ and AFE ordering in squaric acid. 11 While these organic acids represent single-component FE and AFE materials, respectively, Horiuchi and co-workers also reported a fascinating example of two-component ferroelectrics obtained by cocrystallization of organic base phenazine and haloanilic acids. 5a This work demonstrated the predictable formation of FE materials based on the analysis of pK_a values of individual components to ensure the feasibility of proton transfer in the solid state.

Despite the potential for concerted proton displacements in cocrystals of organic acids and bases, the realm of organic FE and AFE materials remains relatively narrow, in large part due to the often unpredictable effects of crystal packing that lead to annihilation of local polarity induced by the acid-base proton transfer. Herein, we demonstrate the synthesis of a new organic AFE based on the combination of squaric acid (H₂sq) and 2,3dimethypyrazine (2,3-Me₂pyz). A distinct feature of this AFE material is the partitioning of molecular layers in its crystal structure into regions that feature either van der Waals interactions between weakly polar methyl groups or extensive hydrogen bonding, due to the asymmetric nature of the 2,3-Me₂pyz molecule with respect to its N···N axis. We use a combination of X-ray and neutron scattering, dielectric and heat capacity measurements, and vibrational spectroscopy to elucidate the behavior of this material and the nature of the electric phase transition observed at 104 K.

EXPERIMENTAL SECTION

Starting Materials. Squaric acid, H₂sq (98%, Oakwood Chemical), and 2,3-dimethylpyrazine, 2,3-Me₂pyz (99%, Alfa Aesar), were used as received.

(2,3-Me₂pyzH⁺)(Hsq⁻)·H₂O (1). H₂sq (1.00 g, 8.77 mmol) was dissolved in 10 mL of deionized water at 50 °C, and neat 2,3-Me₂pyz (0.96 mL, 8.77 mmol) was added dropwise to this solution, resulting in the change of color from colorless to bright-yellow. The solution was cooled to room temperature, and yellow block-shaped crystals began to form within a few minutes. The solution was left undisturbed for 1 day, after which time the crystals were recovered by filtration and dried by suction. Yield = 0.86 g (43%). Anal. Calcd for

C₁₀H₁₂N₂O₅ (1): C, 50.00; H, 5.04; N, 11.66. Found: C, 50.05; H, 4.98; N. 11.58.

X-ray Crystallography. Room-temperature powder X-ray diffraction (PXRD) was performed on a Panalytical XPert Pro diffractometer with Cu K α radiation ($\lambda = 1.54178$ Å). The PXRD patterns were collected over a 2θ range of $10{\text -}60^\circ$ with a step of 0.033° and 0.50 s/step counting time. The data were processed with the CrystalDiffract software.

Single-crystal X-ray diffraction (SCXRD) experiments were performed on a Bruker APEX-II CCD X-ray diffractometer equipped with a graphite-monochromated Mo K α radiation source (λ = 0.71073 Å). A single crystal of 1 was suspended in Paratone-N oil (Hampton Research) and cooled to the desired temperature in a N₂ cold stream. The data sets were recorded as ω -scans at 0.4° step width and integrated with the Bruker SAINT software package. 12 A multiscan empirical adsorption correction was based on multiple equivalent measurements (SADABS).¹³ The space group determination was performed with XPREP, ¹⁴ and the crystal structure solution and refinement were carried out using SHELX. ¹⁵ The final refinement was performed with anisotropic atomic displacement parameters (ADPs) for all non-hydrogen atoms. The methyl and aromatic H atoms were placed in calculated positions and refined in the riding model, while the H atoms involved in hydrogen bonding were located from the difference Fourier electron density map and refined with isotropic ADPs, without restricting the N-H or O-H distances. A summary of pertinent information relating to data collection and crystal structure refinements is provided in Table 1.

Neutron Diffraction. Time-of-flight single-crystal neutron diffraction (SCND) was performed on the TOPAZ diffractometer at the Spallation Neutron Source (Oak Ridge National Laboratory). The crystal was mounted on a MiTeGen loop using a small amount of Super Glue. The data collection strategy was obtained with CrystalPlan. 16 The data were collected for ~60 h at 90 K using 44 sample orientations with 8 C of proton charge each at the beam power of 1 MW and for ~45 h at 230 K using 34 sample orientations with 6 C of proton charge each at the same beam power. Peak integration and data reduction were performed in accordance with previously reported procedures. 17 The positions of H atoms were located from the difference Fourier maps calculated using the neutron diffraction data. The crystal structures were refined anisotropically using SHELX¹⁵ and the ShelXle graphical interface.¹⁸ The details of data collection and crystal structure refinement are summarized in Table 1.

Dielectric Measurements. A single crystal of 1 with the size of 7 \times 4 \times 1.3 mm³ was selected for measuring the dielectric constant as a function of temperature and electric polarization as a function of applied electric field. To obtain a parallel capacitor geometry, Cr/Ag contacts were deposited on two opposite flat surfaces, corresponding to the $\lceil \overline{201} \rceil$ and $\lceil 20\overline{1} \rceil$ faces of the crystal (these faces are parallel to the layers observed in the crystal structure, as will be described below). The deposition had to be performed very carefully, due to the delicate nature of the crystal. First, the edges of the crystal were covered with a Kapton-tape mask, which also attached the crystal to an aluminum plate, for more efficient thermal contact with the cooling plate of the evaporator stage. The assembly was mounted in an evaporator chamber, which was subsequently evacuated for 10 s and then flushed with N2 gas, and this process was repeated five times to minimize the amount of moisture in the chamber. To avoid deterioration of the crystal under high vacuum, the sample stage was first cooled by liquid N_2 to -30 °C under 10^{-2} Torr, and then the pressure was decreased to 3×10^{-7} Torr as the sample stage temperature was lowered to −110 °C. A 5 nm film of chromium followed by a 100 nm film of silver were deposited at the rate of 0.1 nm/s. The temperature of the sample stage increased to -70 °C during the evaporation. After the deposition had been completed, the chamber was flushed with N2 gas for 20 min to warm the sample before opening the chamber. The crystal was flipped, and the deposition process was repeated on the other side. The crystal prepared in such a way had the active electrode area of $\sim 11 \text{ mm}^2$. After making electrical contacts, the assembly was covered with

Table 1. Data Collection and Structure Refinement Parameters for 1 from SCXRD and SCND Experiments

	SCXRD			SC	SCND		
formula:			$C_{10}H_{12}N_2O_5$	(1)			
T, K	90	230		90	230		
CCDC number	1899624	1899171		1898766	1899623		
formula weight	240.22	240.22		240.22	240.22		
space group	$P\overline{1}$	$P\overline{1}$	$A\overline{1}^a$	$P\overline{1}$	$P\overline{1}$		
a, Å	7.9812(6)	6.721(4)	7.967	7.981(2)	6.721(4)		
b, Å	12.5493(9)	7.967(4)	12.633	12.549(3)	7.967(4)		
c, Å	12.7113(9)	10.750(6)	12.723	12.711(3)	10.750(6)		
α , deg	63.345(1)	76.398(5)	64.03	63.35(3)	76.398(5)		
β , deg	73.512(1)	89.550(6)	73.40	73.51(3)	89.550(6)		
γ, deg	83.413(1)	80.515(6)	83.35	83.41(3)	80.515(6)		
V, Å ³	1090.9(1)	551.5(5)	1103.0	1090.9(5)	551.5(5)		
Z	4	2	4	4	2		
crystal color	colorless	yellow		colorless	yellow		
crystal size, mm ³	$0.51 \times 0.51 \times 0.40$	$0.81 \times 0.32 \times 0$	0.24	$3.6 \times 1.35 \times 0.85$	$3.6 \times 1.35 \times 0.85$		
$d_{\rm calc}$, g cm ⁻³	1.463	1.446		1.463	1.450		
μ , mm ⁻¹	0.119	0.118		$0.13084 + 0.0888\lambda$	0.12957 + 0.0879		
λ, Å	0.71073	0.71073		0.40-3.36	0.40-3.36		
$\theta_{ m max}$ deg	28.47	28.53		78.55	79.03		
total reflns	10012	6204		10119	5223		
R _{int}	0.020	0.031		0.108	0.114		
unique reflns	4954	2557		5879	2796		
parameters refined	334	173		524	297		
restraints used	0	0		0	0		
R_1 , $wR_2 \left[I > 2\sigma(I)\right]^b$	0.039, 0.117	0.043, 0.104		0.084, 0.200	0.078, 0.179		
R_1 , wR_2 (all data)	0.051, 0.129	0.070, 0.116		0.084, 0.201	0.079, 0.179		
GOF^c	1.078	1.052		1.339	1.169		
diff. peak/hole	0.31, −0.33e Å ⁻³	0.20, −0.21e Å	-3	2.30, -1.51fm Å ⁻³	1.02, −0.88fm Å [−]		

^aThe alternative nonstandard space group setting is provided for the high-temperature structure to afford the direct comparison to the unit cell of the low-temperature structure (see the discussion in the text). ${}^bR_1 = \sum ||F_0| - |F_c|| / \sum |F_0|$; $wR_2 = [\sum [w(F_0^2 - F_c^2)^2] / \sum [w(F_0^2)^2]]^{1/2}$. ${}^cGOF = [\sum [w(F_0^2 - F_c^2)^2] / (N_{obs} - N_{params})]^{1/2}$, based on all data.

Apiezon-N grease to prevent degradation of the sample and to enhance thermal coupling to the sample platform. The capacitance was measured using a capacitance bridge (Andeen-Hagerling AH2700A) at AC electric field frequencies from 0.2 to 20 kHz. The dielectric constant was obtained from the capacitance by approximating an infinite parallel capacitor geometry. The temperature was varied at 1 K min⁻¹. The electric polarization was measured as a function of electric field at 2.5 and 200 K with the maximum applied voltages of 3 and 2 kV, respectively.

Thermal Analysis. Heat capacity measurements were performed on a 3.89 mg pellet of 1 in the temperature range from 300 to 2 K, using the Physical Property Measurement System (Quantum Design). Apiezon-N grease was used to thermally couple the sample to the platform of the calorimeter. The contribution of the platform, including the grease, was measured independently and subtracted from the total heat capacity data. Simultaneous differential scanning calorimetry and thermogravimetric analysis (SDTA) were performed on a 7.52 mg powder sample of 1 contained in an alumina crucible. The measurement was carried out on a TA Instruments SDT 600Q analyzer under a 100 mL min⁻¹ flow of Ar gas, in the temperature range from 300 to 873 K and at a 5 K min⁻¹ heating rate.

UV–Visible Spectroscopy. The spectrum was collected on a microcrystalline sample of 1 at room temperature, using an Edinburgh FLS980 spectrometer with the integrating sphere accessory. Light output from a housed 450 W Xe lamp was passed through a single grating (1800 l/mm, 250 nm blaze) Czerny-Turner monochromator and then into the integrating sphere containing the powder sample or scattering reference (BaSO₄). The output from the integrating sphere was passed through a single grating (1800 L/mm, 500 nm blaze) Czerny-Turner and finally detected by a Peltier-cooled Hamamatsu R928 photomultiplier tube. Synchronous spectral scans were

performed with both excitation and emission monochromators, with zero wavelength offset, stepping through the preset spectral range. Absorbance was then calculated using Edinburgh's F900 software package.

Infrared Spectroscopy. A polycrystalline sample of 1 was mixed with KBr for transmittance Fourier transform infrared spectroscopy experiments. The measurements were performed on a Bruker Equinox 55 spectrometer equipped with a microscope and a low-profile cryostat (550–7500 cm⁻¹; 4.2–300 K). The middle infrared frequency range was examined to reveal hydrogen-bonding effects. Mode assignments were made using lattice dynamics calculations performed with Spartan, as well as by comparison with literature data. Traditional fitting techniques were employed as appropriate.

Raman Spectroscopy. Raman spectra were collected on a 1 mm thick, pelletized sample of 1, using an Acton SP2500 spectrometer with 1200 g mm $^{-1}$ grating and a 100 μ m entrance slit, providing 3 cm $^{-1}$ resolution. The measurements were performed in the temperature range from 30 to 150 K. The sample was mounted on a copper coldfinger inside a continuous-flow He cryostat. Spectra were recorded from in the 90–3200 cm $^{-1}$ range in quasi-backscattering geometry with nonpolarized 532 nm light. A long-pass edge filter was used to attenuate elastically scattered light. A liquid nitrogen cooled Si CCDC was used for detection. The power incident of the sample was around 2 mW.

■ RESULTS AND DISCUSSION

Synthesis and Stability Studies. Compound 1 was obtained by a reaction between H₂sq and 2,3-Me₂pyz in water in a 1:1 molar ratio. Bright-yellow X-ray quality crystals (Figure S1) grew from the obtained yellow solution within 30 min at

room temperature. The typical crystals were elongated plates, with the long edge often exceeding 1 cm. The crystals are airand moisture-stable and remain intact for prolonged periods if kept in a closed container. Upon exposure to air, 2,3-Me₂pyz and H₂O gradually sublime from the lattice over the course of several days, resulting in the formation of pure H₂sq. Heating a powdered sample of 1 to 50 °C under vacuum accelerates the decomposition process, producing pure H2sq after 20 h, as confirmed by PXRD patterns recorded before and after the decomposition (Figure S2). Simultaneous differential scanning calorimetry and thermogravimetric analysis (SDTA) showed the loss of 2,3-Me₂pyz and H₂O beginning at room temperature and lasting until approximately 425 K, at which point 48.7% of the initial mass remained, in good agreement with the expected mass of 47.5% for the pure H₂sq residue. The remaining H₂sq is then stable until decomposition at 525 K (Figure S3).

On the basis of the observed behavior of 1, its crystals were stored in capped glass vials to prevent any degradation prior to their characterization with diffraction and other physical methods.

Dielectric Properties. The temperature-dependent capacitance measurements on a single crystal of 1 were performed to extract the complex dielectric constant, $\varepsilon(\omega) = \varepsilon'(\omega) +$ $i\varepsilon''(\omega)$. The data analysis revealed a sharp decrease in the real part (ε') of the dielectric constant below ~115 K (Figure 1),

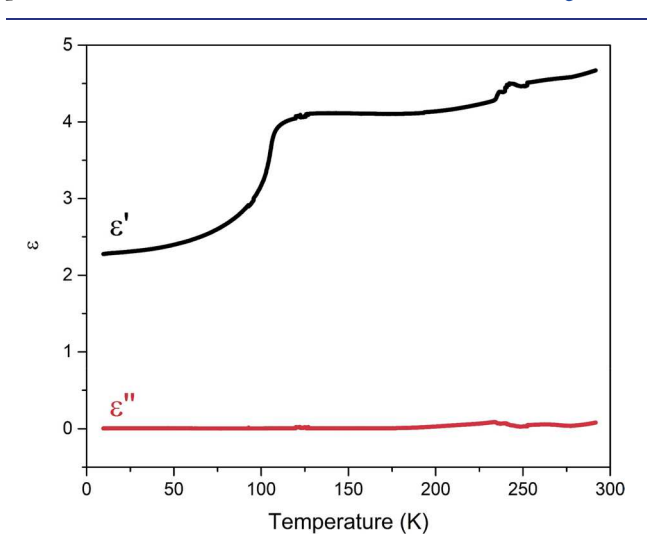


Figure 1. Temperature dependence of the real (ε') and imaginary (ε'') parts of the dielectric constant measured on a single crystal of 1 at the applied AC electric field of the amplitude 15 V and the frequency 2 kHz.

while the imaginary part (ε'') remained near zero over the entire temperature range. The anomaly in the dielectric signal did not exhibit any notable frequency dependence (Figure S4). The pyroelectric current measured near the transition temperature was negligible, and no spontaneous electric polarization was observed. Furthermore, electric polarization measured at 2.5 K showed linear dependence on the applied electric field and the lack of hysteretic behavior (Figure S5). All of these observations suggest a possible AFE phase transition, 19 which emerges from the spontaneous antiparallel ordering of electric dipoles and leads to the decrease in the macroscopic polarizability. 20 The observation of this dielectric anomaly led us to investigate other temperature-dependent

properties of this material, especially the possible changes in its crystal structure above and below the temperature of dielectric anomaly.

Crystal Structure. To elucidate the mechanism of the possible phase transition, the crystal structure of 1 was determined by a combination of SCXRD and SCND (for hydrogen atom detection) at 90 and 230 K, that is, below and above the observed decrease in the dielectric constant. At 230 K, the material crystallizes in the centrosymmetric triclinic space group $P\overline{1}$ with Z=2. Upon lowering the temperature to 90 K, a supercell with Z = 4 was detected, although the space group remained the same. (As will be shown below, the formation of the superstructure is due to the ordering of H atoms involved in hydrogen bonding.) The relationship between the two structures may also be expressed by considering the high-temperature structure in a nonstandard base-centered space group $A\overline{1}$, obtained from the standard $P\overline{1}$

lattice by means of a transformation matrix, $\begin{pmatrix} 0 & 1 & 0 \\ -1 & 0 & 1 \\ 1 & 0 & 1 \end{pmatrix}$. This

transformation results in a unit cell with Z = 4, with parameters and volume comparable to those of the low-temperature structure (Table 1). The structural transition leads to the loss of the A-centering, which is equivalent to the doubling of the primitive unit cell observed at 230 K.

The crystal structure of 1 is built of layers (Figure 2a), which are parallel to the (201) planes that correspond to the basal

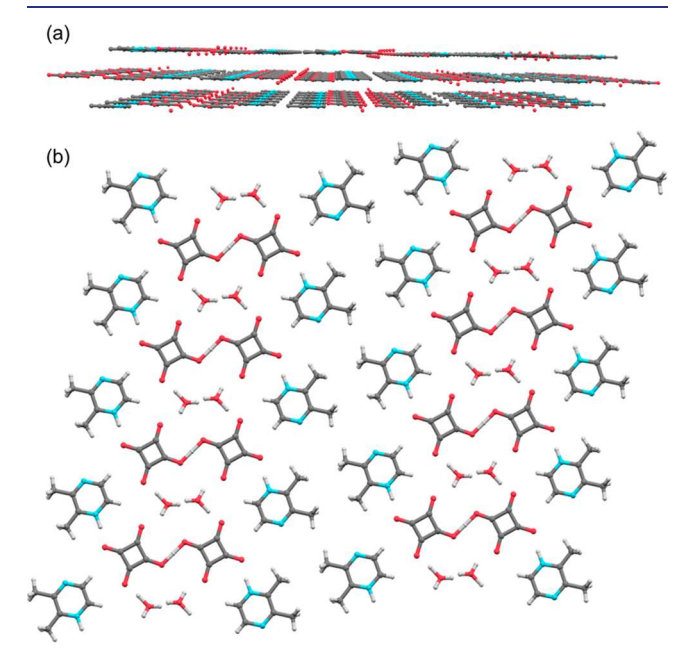


Figure 2. (a) The perspective side view of molecular layers in the crystal structure of 1 at 230 K. Hydrogen atoms are omitted for clarity. (b) The idealized view of the structure of a single layer, which runs parallel to the $(\overline{201})$ plane, showing the separation of the structure into regions lined with methyl groups and regions of extensive hydrogen bonding. Color scheme: O = red, N = blue, C = dark gray, H = light gray.

faces of the plate-like crystals. At 230 K, the distance between adjacent layers is 3.092 Å. In each layer, the base and acid components alternate in such a way that one can distinguish strips lined with methyl groups alternating with strips featuring extensive hydrogen bonding (Figure 2b). One proton from each squaric acid molecule is transferred to a neighboring 2,3-

Scheme 1. Hydrogen Bonding between Molecular Components in the Crystal Structure of 1 at 230 K (a) and 90 K (b)a

(a)
$$H_{(5B)}$$
 $H_{(5B)}$ $H_{(2)}$ $H_{(2)}$ $H_{(3)}$ $H_{(1)}$ $H_{(1)}$

^aThe hydrogen bonds that become ordered at lower temperatures are highlighted with red color. The crystallographic numbering is indicated only for the most important atoms involved in hydrogen bonding. The full atom numbering scheme and atomic displacement ellipsoids are provided in Figure S6.

Table 2. Distances between Atoms Involved in Hydrogen Bonding in the Structure of 1 from SCND^a

	d(B–A), Å		<i>d</i> (B−H), Å		d(H···A), Å	
hydrogen bond (B-H···A)	90 K	230 K	90 K	230 K	90 K	230 K
N(1)-H(1)···O(1)	2.625(3)	2.640(3)	1.080(5)	1.095(5)	1.583(6)	1.549(5)
	2.655(3)		1.093(5)		1.536(6)	
$O(3)-H(3)\cdots O(3)'$	2.512(6)	2.485(5)	1.056(8)	1.243(3)	1.457(9)	1.243(2)
$O(5)-H(2)\cdots O(2)$	2.445(4)	2.544(4)	1.339(8)	1.090(9)	1.111(8)	1.458(9)
	2.677(5)		0.994(7)		1.685(7)	
$O(5)-H(5B)\cdots O(5)'$	2.569(6)	2.552(7)	1.552(8)	0.92(1)	1.018(8)	0.92(1)
$O(5)-H(5A)\cdots O(4)$	2.651(6)	2.669(5)	0.982(9)	0.985(7)	1.76(1)	1.783(7)
	2.709(6)		0.986(9)		1.821(1)	

^aThe labels B and A indicate the N and/or O atoms involved in the hydrogen-bonding pairs.

Me₂pyz molecule, resulting in the formation of 2,3-Me₂pyzH⁺ ions. The protonated side of the 2,3-Me₂pyzH⁺ cations is oriented toward the region of hydrogen bonding, while the side with methyl substituents forms the methyl-lined strip. The protonated N atoms form asymmetric hydrogen bonds to the Hsq^- anions, with the $N(1)-H(1)\cdots O(1)$ distance of 2.640(3) Å at 230 K. Further, the region of extensive hydrogen bonding is composed of the Hsq^- anions and water molecules (Scheme 1 and Table 2). At 230 K, we observe a symmetric H-bonded dimer of the hydrosquarate anions, $(Hsq_2)^{3-}$, with the

bridging proton appearing on the inversion center and the $O(3)\cdots H(3)\cdots O(3)'$ distance of 2.485(5) Å. One of the hydrosquarate protons has been transferred from this dimer to the neighbor water molecules, resulting in a protonated dimer of water molecules, $(H_5O_2)^+$. Thus, in the crystal-chemical formulation, the PE phase can be represented as $(2,3-Me_2pyzH^+)_2(Hsq_2^{3-})(H_5O_2^+)$. The protonated water dimer forms asymmetric H-bonds to the adjacent $(Hsq_2)^{3-}$ dimers, with the $O(5)-H(5)\cdots O(2)$ distance of 2.544(4) Å. The proton H(5B), which participates in an asymmetric H-bond

between water molecules with the O(5)-H(5B)···O(5)' distance of 2.552(7) Å, is disordered over two equally occupied positions. This suggests that the protons H(2) and H(3), which are involved in H-bonding of the $(Hsq_2)^{3-}$ dimer, undergo dynamic shifts between the corresponding O atoms, so that when the H(3) proton is shifted closer to one of the hydrosquarate anions, then this anion transfers its H(2) proton closer to the water molecule, which gives up its H(5B) proton to the next water molecule, that then transfers its proton closer to the next hydrosquarate anion, which in turn causes the shift of the H(3) proton to the other hydrosquarate unit in the dimer, and so on. Such a dynamic picture is additionally supported by the enlarged ADPs of the H(2), H(3), and H(5B) atoms (Figure S6a). We would like to note that the refinement of these ADPs gave reliable results with both the SCND and the SCXRD data.

Upon lowering the temperature from 230 to 90 K, the distribution of protons changes substantially, as revealed by SCND. (The non-hydrogen parts of the structure obtained from SCXRD experiments were used as initial models when refining H atom parameters against SCND data.) While the proton that bridges the Hsq anions is shared equally between them at 230 K, this local symmetry is broken at 90 K, as the proton is shifted toward one of the O atoms, forming the asymmetric O(3)-H(3)···O(3)' bridge with O-H distances of 1.056(5) and 1.457(6) Å, respectively (Scheme 1b). The Hsq⁻ anion that "gave up" the H(3) proton in this bonding is now observed to acquire an outer H(2) proton from the neighbor water molecule, while the Hsq- that acquired the H(3) proton transfers its outer H(2) proton to another water molecule. Accordingly, the H(5B) proton involved in Hbonding between the water molecules has become completely ordered, forming an asymmetric H-bond. The metrics of the asymmetric $O(2)-H(2)\cdots O(5)$, $O(5)-H(2)\cdots O(2)$, and $O(5)-H(5B)\cdots O(5)'$ bridges can be found in Table 2. As a result of this ordered H-bonding, the SCND experiment revealed the formation of a supercell with about 2 times larger volume relative to the volume of the unit cell observed at 230

The ordering of protons within each layer also leads to "dimerization" of the layered structure, as shorter (\sim 2.80 Å) and longer (\sim 3.18 Å) interplanar separations alternate in the 90 K structure, in contrast to the uniform interplanar separation of \sim 3.09 Å in the 230 K structure. The layers are oriented parallel to the ($\overline{2}$ 01) lattice plane in the 230 K structure, which is transformed to the (03 $\overline{1}$) plane in the 90 K structure.

An examination of the crystal packing in the 90 K crystal structure reveals that the protons are shifted in a concerted fashion within the hydrogen-bonded region, producing a net in-plane dipole moment, while the protons of the next hydrogen-bonded region shift to produce a dipole moment in the opposite direction (Figure S7). Thus, because of the structural phase transition, net dipole moments formed in the adjacent hydrogen-bonded regions cancel each other, which explains the observed drop in the dielectric constant and suggests the occurrence of an AFE phase transition. The proton redistribution can also be described with the following reaction scheme:

[2,3-Me₂pyzH⁺]₂[sq···H···sq]³⁻[H₂O···H···OH₂]⁺

$$\rightarrow 2[2,3-Me2pyzH+][Hsq-][H2O]$$
AFF state

where the high-temperature PE state features delocalized protons in the hydrogen-bonded dimers, $\mathrm{Hsq_2}^{3-}$ and $\mathrm{H_5O_2}^+$, while the low-temperature AFE state contains only localized protons.

Such description of the PE \rightarrow AFE phase transition also justifies the change in color from yellow in the PE state (Figures S1 and S8) to colorless in the AFE state. On the basis of the reported calculations of the electronic structure of squaric acid and pyrazine derivatives,²¹ we expect the highest occupied molecular orbitals, HOMO and HOMO-1, to be represented by π -orbitals of 2,3-Me₂pyzH⁺ and the lowest unoccupied molecular orbitals, LUMO and LUMO+1, to correspond to π^* -orbitals of Hsq⁻. Thus, the lowest-energy optical absorption bands correspond to charge transfer from the cation-based HOMO/HOMO-1 to the anion-based LUMO/LUMO+1. The involvement of the Hsq⁻ anions in delocalized hydrogen bonding should lower the energy of LUMO and LUMO+1, while the loss of such delocalization will have an opposite effect, shifting the absorption bands completely to the UV region, which explains the loss of color by crystals of 1 in the AFE phase.

Thermodynamics of the Phase Transition. Heat capacity (C_p) measurements revealed a broad anomaly in the region of the structural phase transition (Figure 3). The

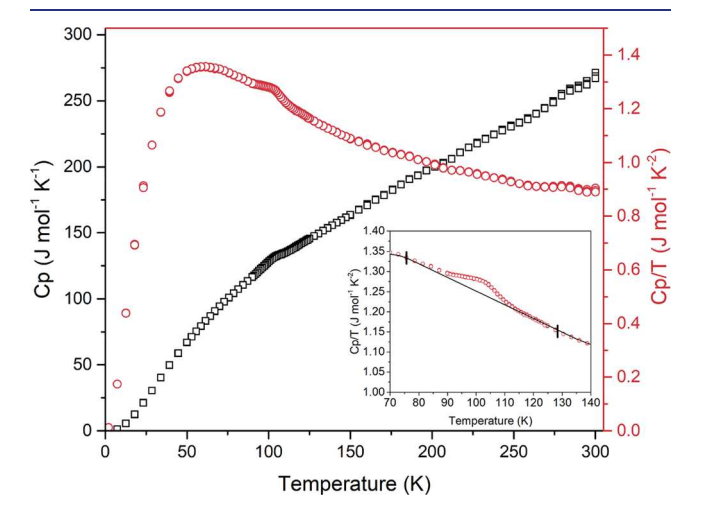


Figure 3. Temperature dependence of C_p and C_p/T measured on a pelletized powder sample of 1. The black line in the inset shows the extrapolated baseline, while the vertical black lines mark the beginning and end points of the integrated region.

change in entropy due to this phase transition, $\Delta S_t = \int \frac{\Delta C_p}{T} \, \mathrm{d}T$, was found by numerical integration of the C_p/T versus T curve after subtracting a baseline extrapolated from the regions above and below the C_p anomaly (Figure 5, inset). The procedure resulted in $\Delta S_t = 0.55 \,\mathrm{J \; mol^{-1} \; K^{-1}}$. On the basis of the Boltzmann–Planck formula, $\Delta S_t = R \,\mathrm{ln} \; N$, where R is the ideal gas constant and N is the ratio of possible states in the high-temperature phase to those in the low-temperature phase, values of N=2 and $\Delta S_t=5.76 \,\mathrm{J \; mol^{-1} \; K^{-1}}$ are expected for an ideal 2-fold order—disorder phase transition. The significantly smaller experimental value of ΔS_t

Journal of the American Chemical Society

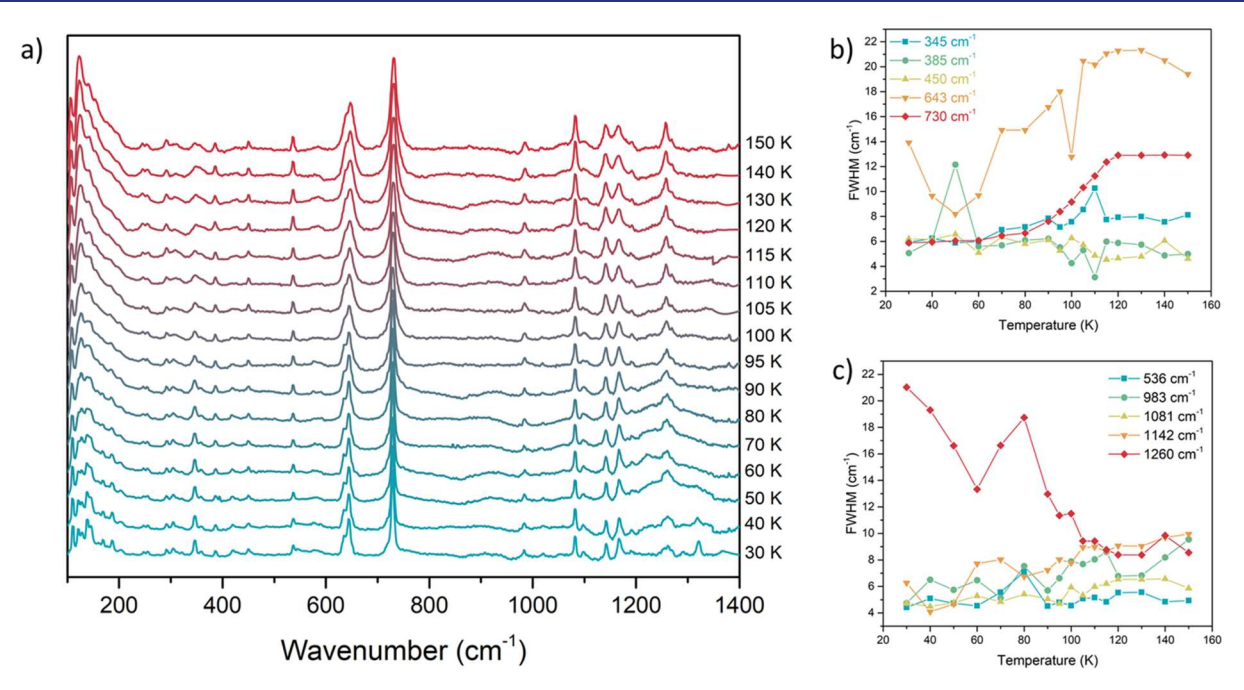


Figure 4. Variable-temperature Raman spectra of 1 collected between 30 and 150 K (a) and temperature dependence of the full-width at half-maximum for peaks assigned to the H₂sq fragments (b) and the 2,3-Me₂pyz fragments (c).

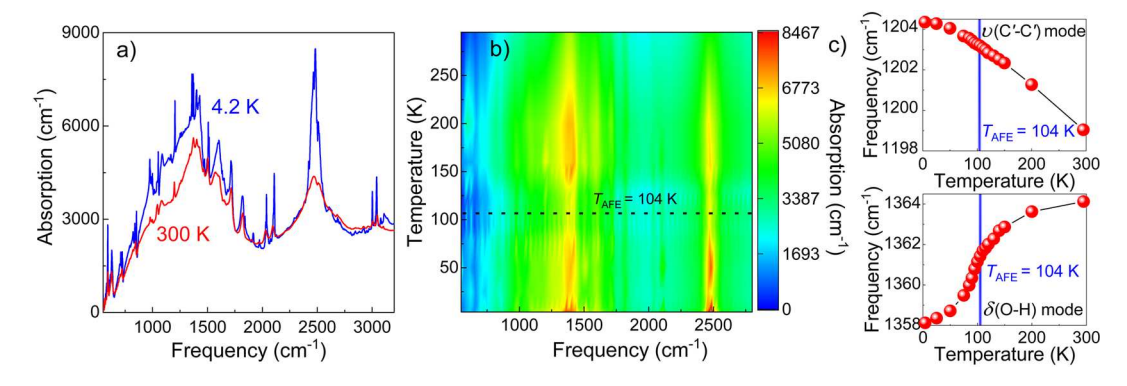


Figure 5. (a) Middle-infrared spectrum of 1 at 295 and 4.2 K. (b) Contour plot of the infrared response of 1 as a function of temperature highlighting line width effects across the 104 K transition. (c) Frequency versus temperature plots for the $\nu(C'-C')$ and $\delta(O-H)$ vibrational modes (see the text for a detailed discussion).

suggests that the mechanism of this AFE phase transition cannot be thought of as the simple ordering of protons. Previous studies of the heat capacity anomaly around the AFE phase transition temperature in pure H_2Sq found $\Delta S_t = 0.228$ J mol⁻¹ K⁻¹, which similarly deviates from the value of 11.28 J mol⁻¹ K⁻¹ expected for two protons ordering per molecular unit.²² On the basis of the investigation of isotope-dependent effects on the FE transition in KH_2PO_4 , it was proposed that the suppression of the experimentally determined values ΔS_t might be due to tunneling terms unaccounted by the simple Boltzmann–Planck model.²³ The suppression of the ΔS_t value might also stem from glassy effects in the phase transition. In the present case, however, such effects are negligible, because the dielectric signal at the phase transition does not show any dissipation, as can be judged from the near-zero value of the out-of-phase dielectric constant (Figure 1a).

Vibrational Spectroscopy. Raman spectra collected over the 30–150 K temperature range (Figure 4a) resemble a combination of the spectra for pure H_2Sq^{24} and 2,3-Me₂pyz, ²⁵ allowing straightforward assignment of the vibrational bands

(Table S2). The positions of all observed peaks are essentially independent of temperature, suggesting the structural phase transition does not impact the strength of intramolecular bonds. Several peaks, however, exhibit a significant decrease in the full-width at half-maximum (fwhm) as the temperature is lowered (Figure 4b), indicating an increased ordering of atomic positions associated with these frequencies. In particular, the fwhm of the band assigned to the $\delta(C'O')$ A_1 mode in squaric acid follows the phase transition seen in the dielectric measurements. The bands assigned to the 2,3-Me₂pyz moieties, in general, lack similar temperature dependence of the fwhm (Figure 4c), with the exception of the 1260 cm⁻¹ band, the intensity of which varied greatly due to the broad underlying absorption feature observed in the corresponding region at lower temperatures (Figure 4a).

The infrared response of 1 was also examined as a function of temperature. Similar to the Raman spectra, the vibrational modes derive from those of the H₂Sq²⁴ and 2,3-Me₂pyz²⁵ molecules. The room-temperature spectrum also shows a strong charge transfer band centered at 1400 cm⁻¹ (Figure 5a).

Evidence for assignment of the broad structure as a low-energy charge transfer band comes from the derivative-like (Fano) line shape of the superimposed vibrational modes. The charge transfer band gains oscillator strength with decreasing temperature. Examination of the contour plot (Figure 5b) reveals that the charge transfer band narrows across the PE \rightarrow AFE phase transition temperature ($T_{\rm AFE}$). These line width changes, on the order of 10%, recover fully away from $T_{\rm AFE}$. At the same time, the vibrational features sharpen with decreasing temperature. Vibrational line width trends are consistent with decreasing thermal fluctuations, as evidenced by the Raman scattering and the behavior of ADPs already discussed in the text, with a distinct narrowing near the 104 K AFE transition (Figure 5b).

We also should point out that several vibrational modes soften with decreasing temperature. This is a common signature of enhanced hydrogen bonding.²⁷ As an example, we track two different vibrations associated with H2Sq as a function of temperature. The A_1 symmetry $\delta(O-H)$ mode softens with decreasing temperature (Figure 5c). The softening may also be connected to the symmetric ↔ asymmetric positioning of the H atom in the O···H···O pathway. Three other vibrational modes, the B_1 symmetry $\pi(O-H)$, B_2 symmetry $\delta(O-H)$, and B_2 symmetry $\nu_{as}(C'=O')$ at 977, 1375, and 1822 cm⁻¹, respectively, follow the same trend, suggesting that they are also involved in hydrogen-bond driven proton transfer in 1. In contrast, the upper panel of Figure 5 displays the position of the A_1 symmetry $\nu(C'-C')$ mode of H₂Sq as a function of temperature. The low-temperature hardening is a typical anharmonic response, and there is no sensitivity to $T_{
m AFE}$ within our resolution. The majority of H₂Sq²⁴ and 2,3-Me₂pyz²⁵ modes behave similarly, suggesting that they do not play a major role in the proton transfer in this system.

CONCLUDING REMARKS

The cocrystallization of 2,3-Me₂pyz and H₂sq provides a remarkable example of an AFE ordered phase. The asymmetric nature of the 2,3-Me₂pyz molecule with respect to the N···N axis forces the partitioning of the resulting layered structure of (2,3-Me₂pyzH⁺)(Hsq⁻)·H₂O (1) into regions lined with methyl groups and regions that feature extensive hydrogenbonded interactions between deprotonated Hsq anions and cocrystallized water molecules. The presence of these hydrogen-bonded regions eventually leads to the spontaneous AFE ordering at 104 K. The phase transition was conclusively confirmed by the combination of neutron and X-ray diffraction, dielectric and heat capacity measurements, and vibrational spectroscopy. The nature of the crystal structure of 1 and the mechanism of AFE ordering hint at a potentially promising approach to the design of new organic ferro- or antiferroelectrics. Other acid-base combinations can be explored, featuring components conducive to the separation of the structure into regions with distinctly different character of intermolecular interactions, whereas the size of the substituents on the molecular components can be systematically varied to arrive at different compositions and structural topologies. Efforts in this direction are currently underway in our laboratories.

ASSOCIATED CONTENT

S Supporting Information

The Supporting Information is available free of charge on the ACS Publications website at DOI: 10.1021/jacs.9b04473.

A single crystal of 1 at room temperature, PXRD patterns of 1 before and after heating under vacuum, SDTA curves, the temperature- and frequency-dependent real part of the dielectric constant, additional crystal structure plots, the UV-visible spectrum, the hydrogen-bonding parameters from SCXRD experiments, and the assignment of vibrational modes (PDF)

X-ray crystallographic data (CIF) X-ray crystallographic data (CIF) X-ray crystallographic data (CIF) X-ray crystallographic data (CIF)

AUTHOR INFORMATION

Corresponding Authors

*dalal@chem.fsu.edu *mshatruk@fsu.edu

ORCID ®

Jeff Lengyel: 0000-0002-5053-6263 Xiaoping Wang: 0000-0001-7143-8112 Tiglet Besara: 0000-0002-2143-2254 Luis Balicas: 0000-0002-5209-0293 Kenneth Hanson: 0000-0001-7219-7808 Naresh S. Dalal: 0000-0002-9996-6918 Michael Shatruk: 0000-0002-2883-4694

Present Address

Operatment of Physics, Astronomy, and Materials Science, Missouri State University, 901 South National Avenue, Springfield, Missouri 65897, United States

Note

The authors declare no competing financial interest.

■ ACKNOWLEDGMENTS

We gratefully acknowledge the support of this research project by the National Science Foundation (award CHE-1464955 to M.S. and N.D.) and the Florida State University Council on Research and Creativity (planning grant to M.S. and N.D.). Single-crystal neutron diffraction experiment performed on TOPAZ used resources at the Spallation Neutron Source, a DOE Office of Science User Facility operated by the Oak Ridge National Laboratory, under contract no. DE-AC05-00OR22725 with UT-Battelle, LLC. The dielectric and Raman measurements were performed at the National High Magnetic Field Laboratory (NHMFL), which is supported by the NSF Cooperative Agreement (DMR-1644779) and the State of Florida. L.B. is supported by the Department of Energy Basic Energy Sciences (award DE-SC0002613), and T.S. is supported by the National Science Foundation (award DMR-1606952). Research at the University of Tennessee is supported by the National Science Foundation (DMR-1707846). A.L.B. thanks the PEER program funded by the National Institute of Health (R25GM086761).

REFERENCES

(1) Scott, J. F. Applications of modern ferroelectrics. Science 2007, 315, 954–959. (b) Lines, M. E.; Glass, A. M. Principles and Applications of Ferroelectrics and Related Materials; Oxford University Press: Oxford, UK, 2000; 688 pp.

- (2) Cheong, S. W.; Mostovoy, M. Multiferroics. A magnetic twist for ferroelectricity. *Nat. Mater.* **2007**, *6*, 13–20. (b) Eerenstein, W.; Mathur, N. D.; Scott, J. F. Multiferroic and magnetoelectric materials. *Nature* **2006**, *442*, 759–765. (c) Fiebig, M.; Lottermoser, T.; Meier, D.; Trassin, M. The evolution of multiferroics. *Nat. Rev. Mater.* **2016**, *1*, 16046.
- (3) Granger, P.; Parvulescu, V. I.; Prellier, W. Perovskites and Related Mixed Oxides; Wiley-VCH: Weinheim, 2016; 978 pp. (b) Liu, H.; Yang, X. A brief review on perovskite multiferroics. Ferroelectrics 2017, 507, 69–85. (c) Wu, H.; Xia, W.; Xue, P.; Zhu, X. Perovskite oxide nanocrystals: Synthesis, characterization, physical properties, and applications. Ferroelectrics 2017, 518, 127–136.
- (4) Horiuchi, S.; Tokura, Y. Organic ferroelectrics. *Nat. Mater.* **2008**, 7, 357–366.
- (5) (a) Horiuchi, S.; Kumai, R.; Tokura, Y. Room-temperature ferroelectricity and gigantic dielectric susceptibility on a supramolecular architecture of phenazine and deuterated chloranilic acid. J. Am. Chem. Soc. 2005, 127, 5010–5011. (b) Horiuchi, S.; Ishii, F.; Kumai, R.; Okimoto, Y.; Tachibana, H.; Nagaosa, N.; Tokura, Y. Ferroelectricity near room temperature in co-crystals of nonpolar organic molecules. Nat. Mater. 2005, 4, 163–166. (c) Horiuchi, S.; Kumai, R.; Tokura, Y. A supramolecular ferroelectric realized by collective proton transfer. Angew. Chem., Int. Ed. 2007, 46, 3497–3501. (d) Szafrański, M.; Katrusiak, A.; McIntyre, G. J. Ferroelectric order of parallel bistable hydrogen bonds. Phys. Rev. Lett. 2002, 89, 215507. (e) Katrusiak, A.; Szafrański, M. Disproportionation of pyrazine in NH+···N hydrogen-bonded complexes: new materials of exceptional dielectric response. J. Am. Chem. Soc. 2006, 128, 15775–15785.
- (6) Horiuchi, S.; Kobayashi, K.; Kumai, R.; Ishibashi, S. Proton tautomerism for strong polarization switching. *Nat. Commun.* **2017**, *8*, 14426.
- (7) Litvin, D. B. Ferroelectric space groups. Acta Crystallogr., Sect. A: Found. Crystallogr. 1986, 42, 44–47.
- (8) Shi, P.-P.; Tang, Y.-Y.; Li, P.-F.; Liao, W.-Q.; Wang, Z.-X.; Ye, Q.; Xiong, R.-G. Symmetry breaking in molecular ferroelectrics. *Chem. Soc. Rev.* **2016**, *45*, 3811–3827.
- (9) Kobayashi, K. K. Dynamical theory of the phase transition in potassium dihydrogen phosphate-type ferroelectric crystals. *J. Phys. Soc. Jpn.* **1968**, 24, 497–508.
- (10) Horiuchi, S.; Tokunaga, Y.; Giovannetti, G.; Picozzi, S.; Itoh, H.; Shimano, R.; Kumai, R.; Tokura, Y. Above-room-temperature ferroelectricity in a single-component molecular crystal. *Nature* **2010**, 463, 789–792.
- (11) Feder, J. Two dimensional ferroelectricity. Ferroelectrics 1976, 12, 71–84.
- (12) SMART and SAINT; Bruker AXS Inc.: Madison, WI, 2007.
- (13) Sheldrick, G. M. SADABS; University of Göttingen: Göttingen, Germany, 1996.
- (14) Sheldrick, G. M. XPREP: Space Group Determination and Reciprocal Space Plots; Siemens Analytical X-ray Instruments: Madison, WI, 1991.
- (15) Sheldrick, G. M. Crystal structure refinement with SHELXL. Acta Crystallogr., Sect. C: Struct. Chem. 2015, 71, 3–8.
- (16) Zikovsky, J.; Peterson, P. F.; Wang, X.-P. P.; Frost, M.; Hoffmann, C. CrystalPlan: An experiment-planning tool for crystallography. *J. Appl. Crystallogr.* **2011**, *44*, 418–423.
- (17) Schultz, A. J.; Jorgensen, M. R. V.; Wang, X.; Mikkelson, R. L.; Mikkelson, D. J.; Lynch, V. E.; Peterson, P. F.; Green, M. L.; Hoffmann, C. M. Integration of neutron time-of-flight single-crystal Bragg peaks in reciprocal space. *J. Appl. Crystallogr.* **2014**, *47*, 915—921
- (18) Hübschle, C. B.; Sheldrick, G. M.; Dittrich, B. ShelXle: a Qt graphical user interface for SHELXL. *J. Appl. Crystallogr.* **2011**, *44*, 1281–1284.
- (19) Jain, P.; Dalal, N. S.; Toby, B. H.; Kroto, H. W.; Cheetham, A. K. Order-disorder antiferroelectric phase transition in a hybrid inorganic-organic framework with the perovskite architecture. *J. Am. Chem. Soc.* **2008**, *130*, 10450–10451.

- (20) Dalal, N. S.; Gunaydin-Sen, O.; Bussmann-Holder, A. Experimental evidence for the coexistence of order/disorder and displacive behavior of hydrogen-bonded ferroelectrics and antiferroelectrics. *Struct. Bonding (Berlin, Ger.)* **2006**, 124, 23–50.
- (21) Korkmaz, U.; Uçar, İ.; Bulut, A.; Büyükgüngör, O. Three forms of squaric acid with pyrazine and pyridine derivatives: an experimental and theoretical study. *Struct. Chem.* **2011**, *22*, 1249–1259.
- (22) Barth, E.; Helwig, J.; Maier, H. D.; Müser, H. E.; Petersson, J. Specific heat of the two dimensional antiferroelectric squaric acid. *Z. Phys. B: Condens. Matter Quanta* **1979**, *34*, 393–397.
- (23) Blinc, R.; Svetina, S. Cluster approximations for order-disordertype hydrogen-bonded ferroelectrics. II. Application to KH₂PO₄. *Phys. Rev.* **1966**, *147*, 430–438.
- (24) Baglin, F. G.; Rose, C. B. The infrared and Raman spectra of crystalline squaric acid. *Spectrochim. Acta, Part A* **1970**, *26*, 2293–2304. (b) Ito, M.; West, R. New aromatic anions. IV. Vibrational spectra and force constants for $C_4O_4^{-2}$ and $C_5O_5^{-2}$. *J. Am. Chem. Soc.* **1963**, *85*, 2580–2584.
- (25) Endrédi, H.; Billes, F.; Keresztury, G. Revised assignment of the vibrational spectra of methylpyrazines based on scaled DFT force fields. *J. Mol. Struct.: THEOCHEM* **2004**, *677*, 211–225.
- (26) Musfeldt, J. L.; Kamarás, K.; Tanner, D. B. Infrared studies of the phase transition in the organic charge-transfer salt *N*-propylquinolinium ditetracyanoquinodimethane. *Phys. Rev. B: Condens. Matter Mater. Phys.* **1992**, 45, 10197–10205.
- (27) Jones, B. R.; Varughese, P. A.; Olejniczak, I.; Pigos, J. M.; Musfeldt, J. L.; Landee, C. P.; Turnbull, M. M.; Carr, G. L. Vibrational properties of the one-dimensional, S=1/2, Heisenberg antiferromagnet copper pyrazine dinitrate. *Chem. Mater.* **2001**, *13*, 2127–2134.